Biocompatible Direct Deposition of Functionalized Nanoparticles using Shrinking Surface Plasmonic Bubble

Seunghyun Moon[1], Qiushi Zhang[1], Dezhao Huang[1], Satyajyoti Senapati[2], Hsueh-Chia Chang[1,2], Eungkyu Lee[1*] and Tengfei Luo[1,2,3*]

[1]Department of Aerospace and Mechanical Engineering, University of Notre Dame, Notre Dame, USA

[2]Department of Chemical and Biomolecular Engineering, University of Notre Dame, Notre Dame, USA

[3]Center for Sustainable Energy of Notre Dame (ND Energy), University of Notre Dame, Notre Dame, USA.

[*]Corresponding to: elee18@nd.edu, tluo@nd.edu,

KEYWORDS: Surface bubble, plasmonic, deposition, biosensing, nanoparticle, DNA

ABSTRACT: Functionalized nanoparticles (NPs) are the foundation of diverse applications, such as photonics, composites, energy conversion, and especially biosensors. In many biosensing applications, concentrating the higher density of NPs in the smaller spot without deteriorating biofunctions is usually an inevitable step to improve the detection limit, which remains to be a challenge. In this work, we demonstrate biocompatible deposition of functionalized NPs to an optically transparent surface using shrinking surface plasmonic bubbles. Leveraging the shrinking bubble can enable to mitigate any potential biomolecules degradation by strong photothermal effect, which has been a big obstacle of bridging plasmonic bubbles with biomolecules. The deposited NPs are closely packed in a micro-sized spot (as small as 3 μm), and the functional molecules are able to survive the process as verified by their strong fluorescence signals. We elucidate that the contracting contact line of the shrinking bubble forces the NPs captured by the contact line to a highly concentrated island. Such a shrinking surface bubble deposition (SSBD) is low temperature in nature as no heat is added during the process. Using a hairpin DNA-functionalized gold NP suspension as a model system, SSBD is shown to enable much stronger fluorescence signal compared to the optical pressure deposition and the conventional steady thermal bubble contact line deposition. The demonstrated SSBD technique capable of directly depositing functionalized NPs may benefit a wide range of applications, such as the manufacturing of multiplex biosensors.

INTRODUCTION

The ability to manipulate nanoparticles (NPs) decorated by functional molecules is critically important for a wide range of applications, such as photonics,[1, 2] nanocomposites,[3] energy conversion,[4-6] and especially biosensors.[7] Advanced biosensing techniques, exemplified by quantum dot Förster resonance energy transfer (FRET)[8] and surface enhanced Raman spectroscopy (SERS),[9] are fundamentally based on the interaction between NPs and functional molecules. As point-of-care (POC) assays become increasingly demanded, diagnosis techniques based on miniaturized microfluidic chips[10-12] with advanced sensors are being developed aimed at analyzing and quantifying small amounts of analytes. For nucleic acid sensors, exponential amplification reactions are usually required to make low target concentration detectable, but they can be incompatible with POC assays due to its time-consuming nature and the requirement of sophisticated laboratory equipment. In addition, such reactions are not applicable to other targets like proteins, ions and lipids.[7] A more commonly applicable strategy is to concentrate targets in the analytes and deposit them onto a surface with pre-fabricated biomarker detectors. Depending on the sensing mechanism of a chip, fabrication processes using expensive equipment such as vacuum deposition, dry/wet etching and lithography may be required, which inevitable impose a cost barrier for large scale applications.[13, 14] It is thus beneficial to directly concentrate NPs that capture targets in solution onto substrates for sensing purposes.

Techniques using nanochannels,[15-17] magnetic nanobeads,[18, 19] evaporation[20] and Langmuir-Blodgett films[21] have been explored to concentrate and deposit suspended particles to surfaces, but depositing them precisely to designated locations, which is important for applications like multiplexing sensors, are still challenging. Previous studies show that fluid flow around an photothermally generated surface bubble can be a promising deposition methods with precision.[22-

[24] The phenomena involved in this process have been extensively studied.[22, 25-30] Due to light absorption of metallic nanostructures fabricated on a surface, a spatially localized laser beam is capable of heating-up the focal area so much that a vapor bubble can be created[31] and the temperature gradient around the bubble leads to a Marangoni flow.[32-34] Such a flow near the bubble draw NPs in the suspension to the vapor-liquid interface acting as a trap to capture the NPs. The flow eventually pushes the NPs towards to the three phase contact line (TPCL) and thus deposit them on the surface. This photothermal bubble deposition process has been explored to deposit materials like polystyrene beads,[22, 26, 33] quantum dots[25, 27] and noble metal NPs,[29, 30, 35] in aqueous environments.

Recently, this approach has been applied to biomarker detection. In this process, high-power lasers (~ hundreds mW-level in the focal area) and light-absorbing plasmonic structures are indispensable for the initial generation of the photothermal bubbles. While the water temperature around the photothermal bubbles under laser illumination is moderately high (~350 K),[27, 35] the laser covered area can have much higher temperatures. In addition, the suspended NPs in the solution can experience intense heating and even supercavitation if the laser wavelength is at the surface plasmon resonance (SPR) peak,[36-41] which would detach any functional molecules from the NP surface immediately. Nevertheless, the Marangoni flow and surface tension, especially at the TPCL, of photothermal bubbles have been studied for capturing and depositing biomarkers like DNA,[42] proteins[43] and microbes.[28, 44] However, to avoid damaging the biomolecules by the high temperature close to the laser-heated area, the size of the deposited region of biomarkers is usually a few times larger than the laser beam size, reducing the concentration ratio and thus sensing signal strength. The thermal problem involved in the photothermal bubble deposition technique limits its application in direct deposition of NP-based biosensors.

In this work, we demonstrate that photothermal bubble can be compatible with the direct deposition of biomolecule-functionalized NPs if we leverage the shrinking process of the bubble when the photo excitation is turned off. Using high speed videography analyses, we elucidate that contracting contact lines of a shrinking bubble force the NPs captured at bubble TPCL to a highly concentrated island with sizes as small as 3 μm. The concentrated NPs are closely packed, and the functional molecules are able to survive the process. Such a shrinking surface bubble deposition (SSBD) technique is low temperature in nature as no heat is added during the process. Using a hairpin DNA-functionalized gold (Au) NP suspension as a model system, SSBD is shown to enable strong fluorescence signal from the deposited NP island on the surface. We have also compared its performance to that from another two deposition mechanisms, including the optical pressure deposition and the conventional stable thermal bubble-induced TPCL deposition. It is found the deposited NPs by optical pressure would damage the functional molecules and show no fluorescence signal when reporters are added. The TPCL deposition can still enable fluorescence detection but the signal strength is notably weaker as the deposited NPs spread over a much larger area (> 30 μm). Through further experiments, we have also elucidated the correlation between the deposited spot size, bubble size and NP concentration in the SSBD process, which is important to its real applications. The SSBD technique demonstrated and physics revealed from this study may benefit a wide range of biosensing applications, such as multiplex biosensors and SERS.

RESULTS AND DISCUSSION

Mechanism of SSBD

When a laser beam is directed into a AuNP suspension, the optical pressure will drive the irradiated NPs toward the surface (**Fig. 1a**) as we elucidated in a recent study.[41] These deposited NPs then act as surface heaters as they continue to convert optical energy into thermal energy, and in the meantime, they are working as nucleation sites for surface bubble nucleation (**Fig. 1a**). In our case, the time delay between laser irradiation and bubble nucleation is found to be ~1s when using a laser power density of ~8.8 mW/μm^2 at the focal plane, which overlaps with the surface of the substrate. It is because of this optical pressure-driven NP deposition that allows us to generate surface bubble without the need of pre-fabricated light absorbers[35] as employed in many other studies.[22, 25-30, 45-49] We note that our laser has a wavelength of 800 nm, which matches the SPR peak of the AuNP used in our experiment (see Method section for more experimental details). With the continued heating of the surface NPs, the surface bubble grows due to both water vaporization and dissolved gas diffusion into the cavity (**Fig. 1b**).[50, 51]

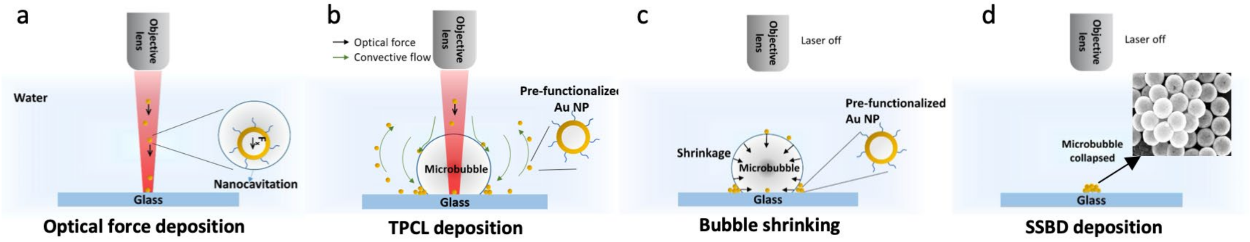

Figure 1. Schematics of **(a)** optical pressure force driving suspended NPs to the surface; **(b)** laser-generated photothermal bubble and the flow surrounding it drives suspended NPs to the three-phase contact line (TPCL); **(c)** laser turned off to allow bubble shrinking which leads to TPCL contraction; and **(d)** concentrated NP island deposited by SSBD due to the complete contraction of TPCL as bubble vanishes. Inset in (d) is a representative scanning electron microscopy image of the SSBD spot.

Particle movement and trapping around a photothermal plasmonic bubble are associated with factors including optical forces, thermophoresis and convective flow.[22, 26, 29] Particularly, the laser-illuminated volume above the bubble is hotter than the bottom due to plasmonic heating of the suspended AuNP.[35] Surface tension gradient at the surface bubble due to such a temperature gradient leads to a Marangoni convection around the bubble (**Fig. 1b**).[33, 52] This flow exerts drag force on the suspended AuNPs and carry them towards the bubble surface. When the NPs are brought to the close proximity of the bubble, the competition between the surface tension and pressure different captures and traps the NPs at the bubble surface. The force due to surface tension pulls the NPs towards the center of the bubble, while the force caused by the pressure difference at the bubble/water interface pushes the NPs outward. Their balance causes the NPs to be trapped.[26, 27, 35] The Marangoni flow at the bubble surface would further drive the trapped NPs to the TPCL. If the bubble is then detached from the surface, the trapped NPs are deposited on the surface as a ring, and this is the mechanism of TPCL deposition using a steady state photothermal surface bubble.[27-29, 35]

However, in our experiment, we do not wait for the bubble to detach, but instead, we discontinue the laser irradiation after the bubble reaches a certain size. With the heat supply absent, the bubble, substrate and the surrounding liquid cool down, and thus the bubble start to shrink (**Fig. 1c**). After the bubble eventually vanishes, a highly concentrated island with closely packed NPs is deposited on the surface (**Fig. 1d)**.

To further elucidate the mechanism behind the SSBD process, we use high-speed videography to characterize the whole bubble shrinking process (**Fig. 2** and Movies S1 and S2). There are two stages in the shrinking of the surface bubble, corresponding to vapor condensation and gas dissolving back to liquid water. The first stage is very fast, on the order of miliseconds.[51, 53] The second stage, gas molecules dissolving back to water, is found to dominate the shrinkage process and the time scale is on the order of hundreds of seconds, which is consistent to other studies.[54] For instance, a bubble of 40 μm in diameter lasts about ~300 s before it eventually vanishes (**Fig. 2a**). An important finding is that the bubble shrinkage is accompanied by the contact-line contraction (**Fig. 2b**). This is believed to be critical to the deposition of highly concentrated NP spot. If the bubble collapses without contact line contraction, the NPs adsorbed on the TPCL should have a ring shape when they are deposited, as found in some other studies.[25] In our case, the deposited site has a filled circular shape.

However, the decrease in contact line width is not continuous. As illustrated schematically in **Fig. 2b** and shown quantitatively in **Fig. 2c**, the bubble initially maintains a nearly constant contact line width while the contact angle increases gradually. When the contact angle reaches a critical value, θ_{cr} (55 ± 1 ° in our case), the contact line width start to decrease rapidly. This phenomenon can be further explained by analyzing the force balance at the TPCL via Young's equation:

$$\gamma_{SL} + \gamma_{LG} cos\theta = \gamma_{SG}, \quad \text{for } \theta \leq \theta_{cr} \tag{1}$$

$$\gamma_{SL} + \gamma_{LG} cos\theta < \gamma_{SG}, \quad \text{for } \theta > \theta_{cr} \tag{2}$$

where γ_{SL}, γ_{LG} and γ_{SG} represent the interface energy of solid-liquid, liquid-gas and solid-gas, respectively (**Fig. 2c**). Due to the tendency to minimize liquid-vapor surface energy, bubble would always like to maintain a spherical shape. When the surface bubble shrinks, the contact line should tend to contract to keep the bubble as spherical as possible. However, the contact line is pinned and thus the bubble comes increasingly non-spherical (i.e., liquid-gas surface energy, γ_{LG}, increases), which leads the contact angle to increase and the surface tension of bubble to build up

(Eq. 1). This continues until the contact line can no longer be pinned by the pinning forces, which eventually leads to the contraction of the contact line (Eq. 2). As shown in Eq. 2, when the contact angle is larger than the critical angle on the hydrophilic substrate, γ_{SG} becomes dominant. This leads to the contraction of the contact line (**Fig. 2b**) and the NPs adsorbed on the TPCL are pulled inward.

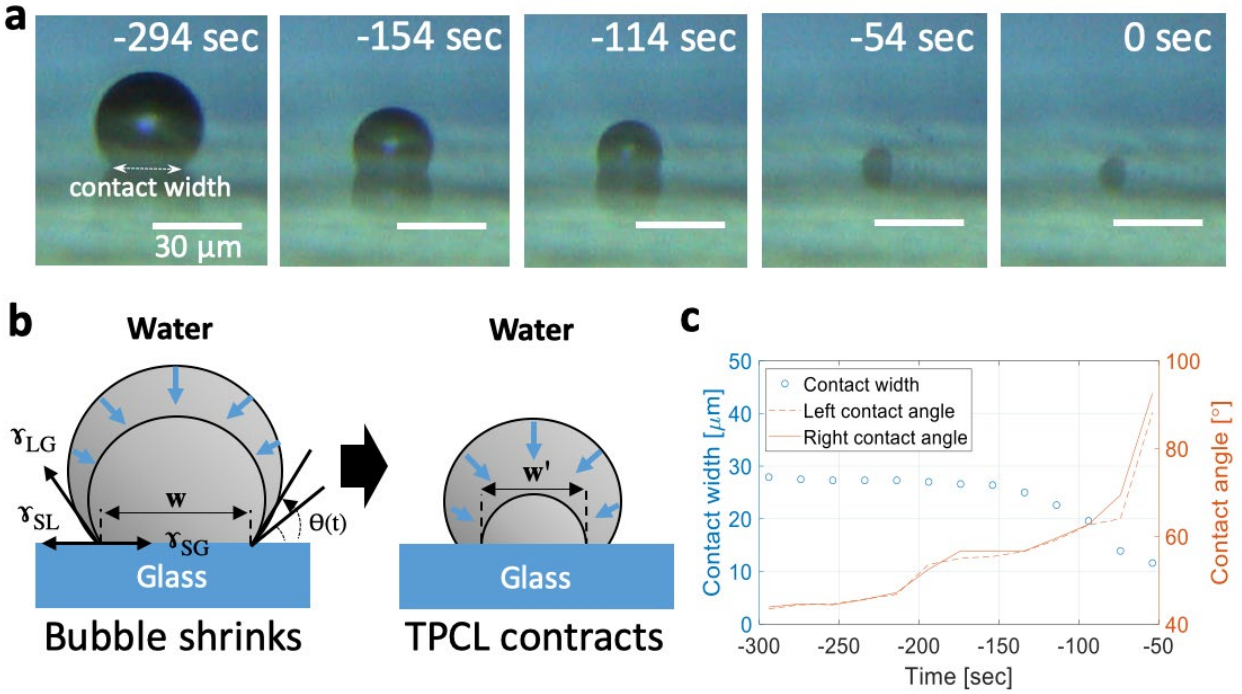

Figure 2. **(a)** Successive optical images from the side view of a typical shrinking bubble on the glass substrate. **(b)** Schematic illustration for of the TPCL contraction during bubble shrinkage. **(c)** Contact width and contact angle as a function of time during the bubble shrinking process.

Verification of the Biocompatibility of SSBD

The above understood mechanism suggests that the NPs captured by the TCPL can be piled into a concentrated spot as the bubble shrinks to vanish and the whole process happens without laser heating. This would maintain the viability of the molecules attached to the NPs. We demonstrate the applicability of this SSBD technique for bio-sensing applications by directly depositing single-stranded DNA (ssDNA)-functionalized core-shell AuNPs onto a bare glass substrate.

NPs made of a silica-core (~100 nm in diameter) and a Au-shell (~10 nm in thickness) are used since they have a SPR peak (~785 nm) matching the wavelength of our excitation laser (see supplemental information). The ssDNA is conjugated to the AuNP surface through the strong goldsulfur bonding[55] (**Fig. 3a**, and see Method section for details). To achieve this bonding, the ssDNA oligonucleotides were custom modified with thiol groups at the 3' end (Integrated DNA Technologies, Inc.), which binds to the gold surface according to the salt aging protocol described by Hurst et al.[56] The ssDNA consists of 35 bases and 57.1% of GC content and is capable of folding so as to form a hairpin loop through complementary hydrogen bonding (**Fig. 3a**).[57] The presence of this secondary structure (i.e., hairpin) at room temperature is beneficial for our purpose because it can provide a binding site of intercalating dyes, such as SYBR Green I (SG I), to confer fluorescence emission.[58] SG I (Invitrogen) is a staining dye that specifically binds to double-stranded DNA and emits green fluorescence. The hairpin structure of our ssDNA provides such a binding site (**Fig. 3a**) as predicted using the IDT SciTools.[59] The estimated free energy (ΔG) is -1.75 kcal/mole and the melting temperature (T_m) is 45.9°C.[59] Thus, the spontaneous hairpin structures at room temperature should allow us to observe florescence signals with SG I added, if the ssDNA survived the SSBD process. The viability of the ssDNA can be further verified by thermal cycling above the T_m, which will break the complementary hydrogen bonds, which will release the fluorescent dye that was intercalated at the hairpin loop and lead to a decrease in fluorescence intensity.

As shown in **Fig. 3b**, green fluorescence signals are apparent from the SSBD-deposited NP spots after SG I was introduced to the solution. When the solution is heated to 50 °C, the signals almost disappear, and when cooled down and SG I re-introduced, fluorescence is seen again despite reduced intensity. **Figure 3c** quantitatively shows the average fluorescence intensity from an array of 20 SSBD-deposited spots, where the error bars are the standard deviation. This results indicates that the signals before and after heating are significantly different. We also note that the intensity decrease in the second thermal cycle (from ~14.5 to ~9.5) potentially suggests that the SSBD technique is even less damaging than heating at 50 ºC for the biomolecules. These results confirmed that the SSBD process can maintain the viability of the functional molecules on NPs, which makes it a technique compatible to biological applications.

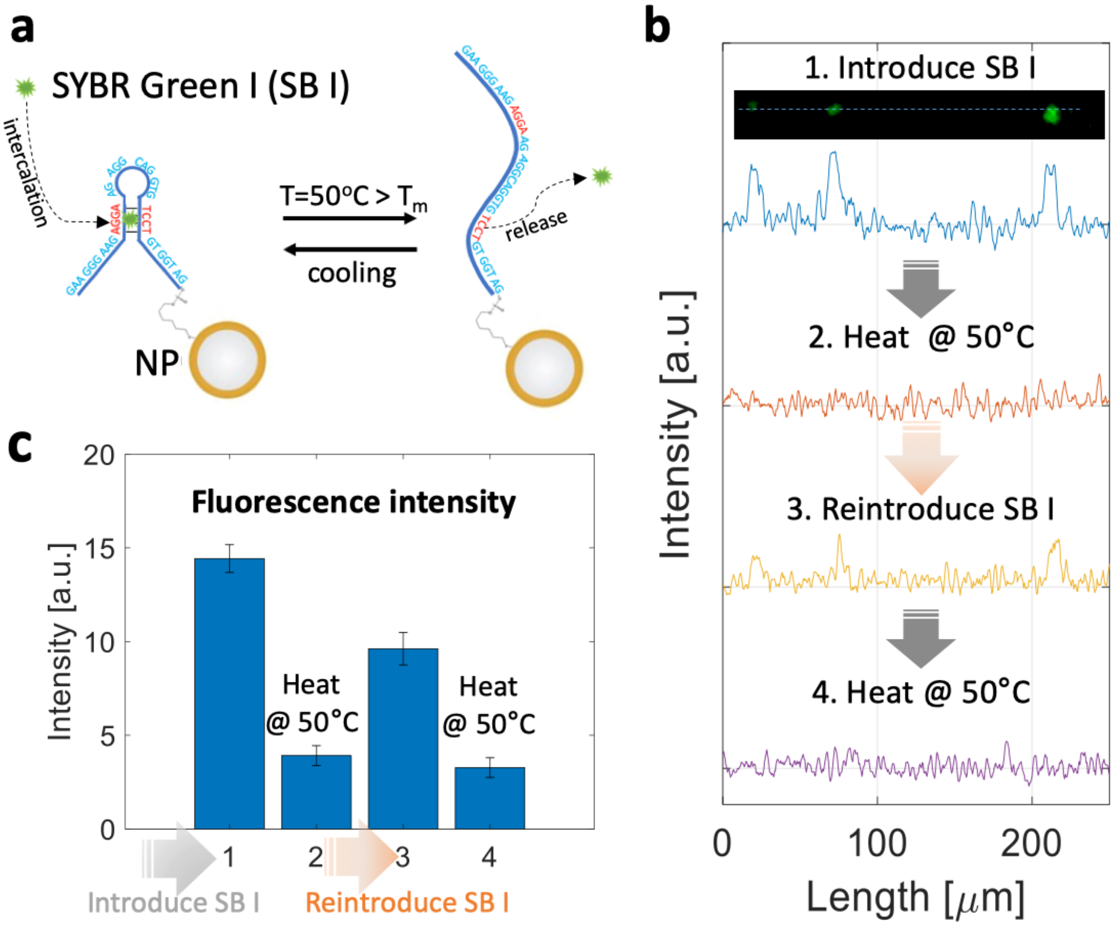

Figure 3. **(a)** Schematics of testing the viability of the ssDNA using its hairpin structure that can use SB I as a reporter. Upon heating, the hairpin structure will open up and the SB I released. (b) Line profiles of the fluorescence signals from the SSBD-deposited ssDNA-AuNP islands in two heating cycles, involving 4 steps: introduction of SG I, release of SG I by heating at 50 °C, reintroduction of SG I, and re-heating. (c) Average fluorescence intensities measured from 20 different SSBD-deposited spots, where the error bars represent the standard deviation.

Comparison with Other Deposition Mechanisms

We further compared the SSBD method to the other two deposition mechanisms mentioned previously (i.e., optical pressure deposition and contact line deposition). In the optical pressure deposition (**Fig. 1a**), the optical force on the NPs drives them to the surface[41] and all deposited NPs are exposed directly to the laser irradiation. We intentionally reduced the laser power density (~3.6 mW/μm^2 at the focal plane) so that no surface bubble is generated within the period of laser irradiation. To produce dense patterns on the glass substrate as shown in **Fig. 4a**, the optical shutter is opened and closed for 30 times at the same location, after which a pattern of about ~20 μm in diameter, similar to the laser diameter, is produced. Survivability of the biological molecules on the AuNP surfaces after deposition is examined by intercalating dye, but fluorescence signal cannot be detected. This result agrees with our expectation considering that the high absorption cross-section (as shown in **Fig. S1**: ~ 2.3×10^{-14} m^2 for the core-shell AuNPs solution[35, 60]) of AuNPs may induce extreme heating of the NPs and even nanocavitation[38, 41] when directly irradiated by the laser at the SPR peak. This would inevitably result in the destruction of ssDNA attached on the NP surface.

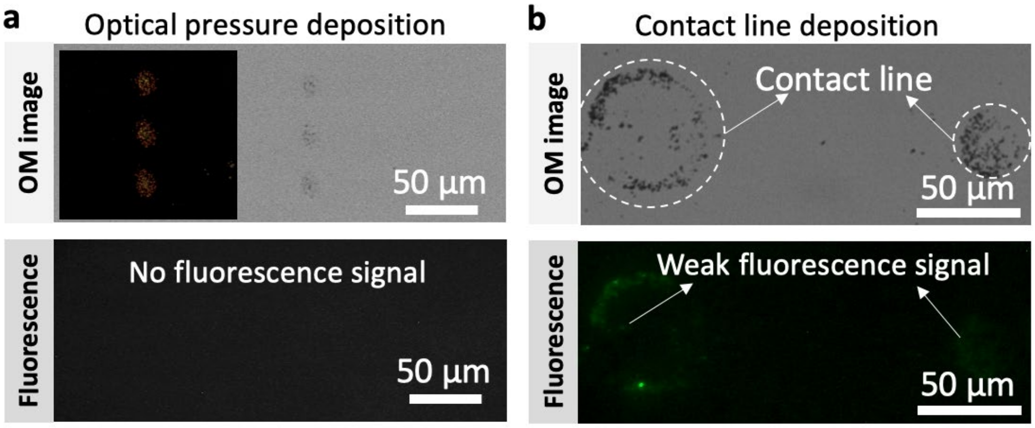

Figure 4. **(a)** Top: Bright and dark field (inset) images of deposited patterns from the optical pressure deposition method (see Fig. 1a for schematic). Bottom: No fluorescence signal can be detected from the deposition spots. **(b)**

Top: Optical microscope image shows deposited AuNPs from the contact line deposition around a steady state photothermal bubble (see Fig. 1b for schematic). Ring-like patterns correspond to the contact line of the thermal bubbles. Bottom: Fluorescence signal is detected using 1s exposure time – the same as that in Fig. 3.

The contact line deposition mechanism leverages the fluid flow around the thermal bubble to capture and immobilize suspended particles at the TCPL (**Fig. 1b**).[25-29] Although this technique is efficient in trapping NPs, maintaining the bubble with continuous laser heating is not desirable as the bubble area is kept at a relatively high temperature which may lead to degradation of biomolecules. In addition, since the contact line ring is usually a few times larger than the laser spot, the concentration of the deposited NPs will be low compared to the SSBD-deposited spots. As shown in **Fig. 4b**, the deposited NP areas are 2-4 times larger than the laser spot size (~20 um) depending on the sizes of bubbles when they detach from the surface. As expected, we also see that the patterns of the deposited NPs are close to rings with higher density at the periphery. The fluorescence signal intensity from the deposited NPs (**Fig. 4b**, bottom) is apparently lower than that from the SSBD-deposited spots (**Fig. 3b**), which can be attributed to the fact that the contact line deposited NPs spread over a larger area and thus lower density.

Controlling the SSBD Process

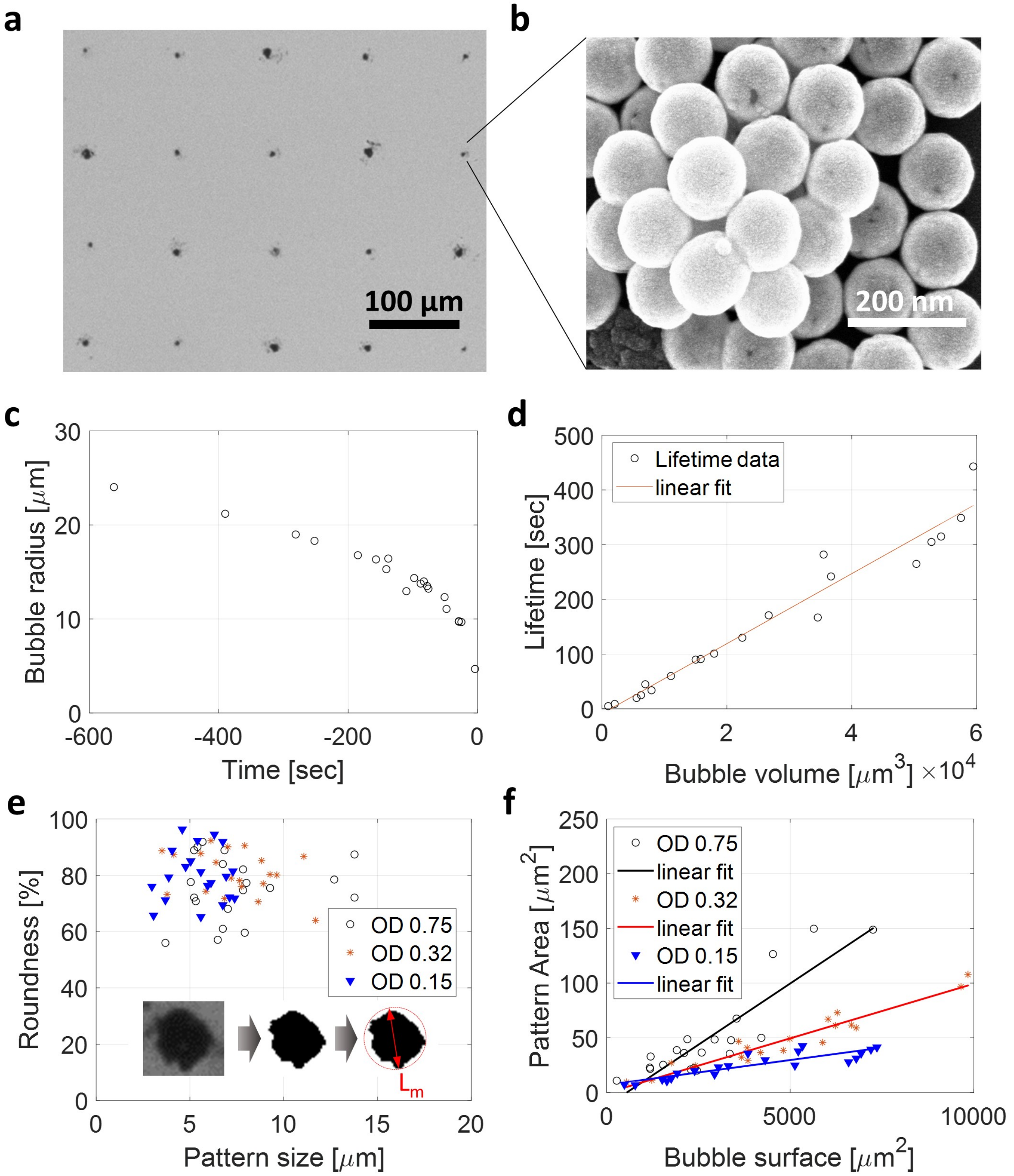

Figure 5. **(a)** An array of 20 micropatterns produced by SSBD using ss-DNA-functionalized AuNP suspension with an optical density (OD) of 0.75 at 800 nm. The peak radii of the bubbles are tuned by controlling the laser illumination times (between 1 ~ 5 sec). **(b)** A typical SEM image of the deposited spot, showing highly concentrated and closely

packed NPs. **(c)** Radius of a bubble as a function of shrinkage time. **(d)** Lifetimes of bubble as a function of the their peak volume. The line fitting indicates that the lifetime shows the power-three dependence. **(e)** Roundness of fabricated patterns as defined in Eq. 4. Three different concentrations (optical density 0.75, 0.32 and 0.15 at 800 nm) of pre-functionalized NP solutions are studied. Inset illustrates how the pattern size (L_{major}) is defined, and the roundness is the ratio between the black area and the area of the peripheric circle (red dashed circle). **(f)** The correlation between surface area of generated bubble and SSBD-deposited pattern area. The reduced dimension (bubble radius and pattern size) also shows linear relation, but it will produce an inaccurate prediction model (see **Fig. S3** and Table S1 for the reduced dimension model).

The ability to control the SSBD process is critical to its future applications. When implementing the SSBD for mass production of sensors, the lifetime of bubble is important because it is the determining factor of the fabrication time scale. We first study the lifetime of bubbles with different peak sizes, which are achieved by varying the illumination time (1-5 s) of the incident laser. We fabricate a 5×4 microarray of patterns on the glass substrate with the pitch of ~100 μm (**Fig. 5a**). In all cases, the SSBD deposited NPs are dense and closely packed (e.g., **Fig. 5b**). Assuming ideal gas and diffusion-governed process, Baffou et al. reported that the lifetime of microbubble (τ_B) can be estimated as:[54]

$$\tau_B = \frac{P_0 K}{6RTD\gamma} a^3 \tag{3}$$

where P_0 is ambient pressure, γ (72×10^{-3} N·m^{-1}) is surface tension, K is Henry's coefficient, R is ideal gas constant (8.31 J·mol^{-1}·K^{-1}), T is temperature of the microbubble, D is diffusion coefficient and a is the radius of the bubble. Based on our measurements, the lifetime of microbubble estimated from videography scales linearly with the volume of the bubble as shown in **Fig. 5d**, which is consistent with the previous research.[54] These results suggest that the SSBD process would have a time scale of seconds to several minutes, depending on the size of the bubble. In mass production, one may generate a large array of bubbles and let them shrink to increase productivity.

It is expected that the size of bubble should directly influence the size of the eventually deposited NP spot size. In a similar vein, controlling the concentration of the NPs in the solution provides another route to tune the amount of NPs the bubble TPCL can capture. To analyze the above two controlling strategies, we prepare three different concentrations of functionalized AuNPs suspensions, including optical densities (OD) of 0.75, 0.32 and 0.15 at 800 nm. At each concentration, we produce 20 bubbles with different peak sizes. The sizes of the bubbles are determined through video analysis, and the images of the deposited AuNP patterns are observed using an optical microscope. To define the size of the pattern, roundness (inset in **Fig. 5e**) is first introduced as:

$$Roundness\ (\%) = \frac{4 \times A_{Au}}{\pi L_m^2} \tag{4}$$

where A_{Au} is the area of the AuNP pattern, and L_m is the length of the major axis in the pattern, which is used to describe the pattern size. **Figure 5e** shows that the patterns all have roundness greater than 50% with a mean value of ~80% and a spread of ~20% (**Fig. S2** for the histogram of roundness). It is also observed that when the NP concentration increases, the average size of the spots increases but the average roundness does not change much. **Figure 5f** shows the pattern area as a function of the surface area of bubble. For each concentration, pattern area and surface area of bubble generally follow a linear relation, with the slope of the linear fit increases with the concentration of the NPs. The fitting parameters are shown in **Table 1** for the three linear curves. We note that the observed linearity between the surface area of bubble and pattern area is more reasonable than the reduced dimension such as bubble radius and pattern size (**Fig. S3**). The NPs attracted by the incident laser beam (Movie S3) thus flow along the bubble surface and eventually are piled into the contact line. Larger surface bubble has more NPs trapped there, thus the SSBD-deposited spot area should scale linearly with the surface area of bubble. Such information is useful for controlling the spot area of the SSBD.

Table 1. Fitting parameters for the surface area of bubble and pattern area shown in Fig. 5f.

OD at 800 nm	Linear fitting		
	Slope	Intercept	R^2
0.75	0.0224	-12.2	0.789
0.32	0.0100	-0.3	0.926
0.15	0.0045	7.1	0.786

CONCLUSIONS

In summary, we have demonstrated a SSBD technique that can deposit bio-molecule-functionalized NPs directly on substrate for biosensing purposes. The key of the SSBD process is its low temperature feature, which maintains the viability of the bio-molecules. The photo-excited thermal bubble captures NPs in the suspension at the TPCL, and when the laser light is turned off, the shrinking bubble leads to the contraction of the contact line, which pulls the captures NPs to a small spot. Such deposited spots show high concentrations of closely packed NPs. We have also tested the optical pressure deposition technique, but it damages the bio-molecules due to the high temperature of the NPs upon laser excitation. The conventional contact line deposition using a steady state thermal bubble shows much larger deposited rings and weaker biosensing signals compared to those of SSBD. We have also shown that by controlling the bubble size and the NP concentration, the SSBD spot area can be tuned. We expect the results from this work to provide new opportunities for direct deposition of functionalized NPs which may greatly contribute to the advancement of lab-on-a-chip based biosensors.

METHODS

Optical setup for nanoparticle deposition

An 800-nm femtosecond pulsed laser (linear polarized Gaussian beam) with a repetition rate of 80.7 MHz and a pulse duration of 200 fs is focused in the pre-functionalized NP suspension using a 20× objective lens with a numerical aperture of 0.42. 2 mL of p-Au NPs is dispersed in the cuvette. The length of the laser beam path in the cuvette is fixed at 4 mm using a PDMS holder. Commercial microscope slide glass (Superfrost® Plus Micro Slide, VWR international, LLC.) is used as a substrate for all experiments.

Preparation of pre-functionalized AuNP

Reduction of thiol-modified DNA was performed using Tris(2-carboxyethyl)phosphine hydrochloride (TCEP) (20 mM). Blending DNA with TCEP reduction agent, the solution was incubated at room temperature for 3 hours. The cleaved DNA was then purified by a NAP-5 column (illustra NAP Columns, GE Healthcare). The purified DNAs were injected to a core/shell AuNP solution (Auroshell, Nanospectra Biosciences, Inc., number density of 2×10^9 /ml) containing 0.01 M phosphate buffer (PB) and 0.01% sodium dodecyl sulfate (SDS). The DNA and AuNPs solution was then incubated at room temperature for 20 min. Concentration of sodium chloride (NaCl) in the DNA/AuNPs solution was increased to 0.05 M by adding a NaCl stock solution (2 M). The solution was then sonicated for 10 sec and incubated for 20 min at room temperature. This process was repeated until the concentration of salt in the solution reached 1 M. The final solution was stored at room temperature for 30 hours. After the incubation step, the suspension containing salt and functionalized AuNPs centrifuged and the supernatant was removed. The NPs were then resuspended in DI water. A total of 5 supernatant removals were carried out by repeating the washing process.

Validation test using intercalating dye

SYBR™ Green I (10,000× concentrate in DMSO, Invitrogen) was diluted (1:50) with phosphate buffered saline (PBS) 1× solution. The deposited patterns were stained using 100 µL of diluted SYBR solution for 20 min. After washing with PBS 4× solution and DI water, the patterns was immersed in a 100 µL of PBS 1× solution. Images were taken by an inverted fluorescence microscope (Eclipse Ti, Nikon). In the validation test, the pre-warmed PBS 1× solution was filled to remove the intercalating die from the DNA and the patterned samples was heated on a hotplate (50 °C) for 15 min.

REFERENCES

(1) Parker, A. R.; Townley, H. E. Biomimetics of photonic nanostructures. *Nature nanotechnology* **2007,** *2* (6), 347.

(2) Lustig, W. P.; Mukherjee, S.; Rudd, N. D.; Desai, A. V.; Li, J.; Ghosh, S. K. Metal–organic frameworks: functional luminescent and photonic materials for sensing applications. *Chemical Society Reviews* **2017,** *46* (11), 3242-3285.

(3) Ong, W.-L.; Rupich, S. M.; Talapin, D. V.; McGaughey, A. J.; Malen, J. A. Surface chemistry mediates thermal transport in three-dimensional nanocrystal arrays. *Nature materials* **2013,** *12* (5), 410-415.

(4) Wang, L.; Yan, R.; Huo, Z.; Wang, L.; Zeng, J.; Bao, J.; Wang, X.; Peng, Q.; Li, Y. Fluorescence resonant energy transfer biosensor based on upconversion-luminescent nanoparticles. *Angewandte Chemie International Edition* **2005,** *44* (37), 6054-6057.

(5) Tao, P.; Ni, G.; Song, C.; Shang, W.; Wu, J.; Zhu, J.; Chen, G.; Deng, T. Solar-driven interfacial evaporation. *Nature energy* **2018,** *3* (12), 1031-1041.

(6) Pang, Y.; Zhang, J.; Ma, R.; Qu, Z.; Lee, E.; Luo, T. Solar-Thermal Water Evaporation: A Review. *ACS Energy Letters* **2020,** *5* (2), 437-456.

(7) Howes, P. D.; Chandrawati, R.; Stevens, M. M. Colloidal nanoparticles as advanced biological sensors. *Science* **2014,** *346* (6205), 1247390.

(8) Clapp, A. R.; Medintz, I. L.; Mattoussi, H. Förster resonance energy transfer investigations using quantum-dot fluorophores. *ChemPhysChem* **2006,** *7* (1), 47-57.

(9) Stiles, P. L.; Dieringer, J. A.; Shah, N. C.; Van Duyne, R. P. Surface-enhanced Raman spectroscopy. *Annu. Rev. Anal. Chem.* **2008,** *1*, 601-626.

(10) Gubala, V.; Harris, L. F.; Ricco, A. J.; Tan, M. X.; Williams, D. E. Point of care diagnostics: status and future. *Analytical chemistry* **2012,** *84* (2), 487-515.

(11) Yang, Y.; Yoon, S. G.; Shin, C.; Jin, H.; Lee, W. H.; Park, J.; Kim, Y. S. Ionovoltaic urea sensor. *Nano Energy* **2019,** *57*, 195-201.

(12) Li, D.; Wang, C.; Sun, G.; Senapati, S.; Chang, H.-C. A shear-enhanced CNT-assembly nanosensor platform for ultra-sensitive and selective protein detection. *Biosensors and Bioelectronics* **2017,** *97*, 143-149.

(13) Park, S.; Lim, J.; Pak, Y. E.; Moon, S.; Song, Y.-K. A solid state nanopore device for investigating the magnetic properties of magnetic nanoparticles. *Sensors* **2013,** *13* (6), 6900-6909.

(14) Wang, P.; Xia, M.; Liang, O.; Sun, K.; Cipriano, A. F.; Schroeder, T.; Liu, H.; Xie, Y.-H. Label-free SERS selective detection of dopamine and serotonin using graphene-Au nanopyramid heterostructure. *Analytical chemistry* **2015,** *87* (20), 10255-10261.

(15) de la Escosura-Muñiz, A.; Merkoçi, A. A Nanochannel/Nanoparticle-Based Filtering and Sensing Platform for Direct Detection of a Cancer Biomarker in Blood. *Small* **2011,** *7* (5), 675-682.

(16) Chou, I.-H.; Benford, M.; Beier, H. T.; Coté, G. L.; Wang, M.; Jing, N.; Kameoka, J.; Good, T. A. Nanofluidic biosensing for β-amyloid detection using surface enhanced Raman spectroscopy. *Nano letters* **2008,** *8* (6), 1729-1735.

(17) Choi, I.; Huh, Y. S.; Erickson, D. Size-selective concentration and label-free characterization of protein aggregates using a Raman active nanofluidic device. *Lab on a Chip* **2011,** *11* (4), 632-638.

(18) Zhang, H.; Yi, Y.; Zhou, C.; Ying, G.; Zhou, X.; Fu, C.; Zhu, Y.; Shen, Y. SERS detection of microRNA biomarkers for cancer diagnosis using gold-coated paramagnetic nanoparticles to capture SERS-active gold nanoparticles. *RSC advances* **2017,** *7* (83), 52782-52793.

(19) Kim, Y.-Y.; Bang, Y.; Lee, A.-H.; Song, Y.-K. Multivalent Traptavidin–DNA Conjugates for the Programmable Assembly of Nanostructures. *ACS nano* **2019,** *13* (2), 1183-1194.

(20) Rabani, E.; Reichman, D. R.; Geissler, P. L.; Brus, L. E. Drying-mediated self-assembly of nanoparticles. *Nature* **2003,** *426* (6964), 271-274.

(21) Kim, F.; Kwan, S.; Akana, J.; Yang, P. Langmuir− Blodgett nanorod assembly. *Journal of the American Chemical Society* **2001,** *123* (18), 4360-4361.

(22) Zheng, Y.; Liu, H.; Wang, Y.; Zhu, C.; Wang, S.; Cao, J.; Zhu, S. Accumulating microparticles and direct-writing micropatterns using a continuous-wave laser-induced vapor bubble. *Lab on a Chip* **2011,** *11* (22), 3816-3820.

(23) Furlani, E. P.; Karampelas, I. H.; Xie, Q. Analysis of pulsed laser plasmon-assisted photothermal heating and bubble generation at the nanoscale. *Lab on a Chip* **2012,** *12* (19), 3707-3719.

(24) Xie, Y.; Zhao, C. An optothermally generated surface bubble and its applications. *Nanoscale* **2017,** *9* (20), 6622-6631.

(25) Fujii, S.; Kanaizuka, K.; Toyabe, S.; Kobayashi, K.; Muneyuki, E.; Haga, M.-a. Fabrication and placement of a ring structure of nanoparticles by a laser-induced micronanobubble on a gold surface. *Langmuir* **2011,** *27* (14), 8605-8610.

(26) Zhao, C.; Xie, Y.; Mao, Z.; Zhao, Y.; Rufo, J.; Yang, S.; Guo, F.; Mai, J. D.; Huang, T. J. Theory and experiment on particle trapping and manipulation via optothermally generated bubbles. *Lab on a Chip* **2014,** *14* (2), 384-391.

(27) Lin, L.; Peng, X.; Mao, Z.; Li, W.; Yogeesh, M. N.; Rajeeva, B. B.; Perillo, E. P.; Dunn, A. K.; Akinwande, D.; Zheng, Y. Bubble-pen lithography. *Nano letters* **2015,** *16* (1), 701-708.

(28) Yamamoto, Y.; Shimizu, E.; Nishimura, Y.; Iida, T.; Tokonami, S. Development of a rapid bacterial counting method based on photothermal assembling. *Optical Materials Express* **2016,** *6* (4), 1280-1285.

(29) Kang, Z.; Chen, J.; Ho, H.-P. Surface-enhanced Raman scattering via entrapment of colloidal plasmonic nanocrystals by laser generated microbubbles on random gold nano-islands. *Nanoscale* **2016,** *8* (19), 10266-10272.

(30) Armon, N.; Greenberg, E.; Layani, M.; Rosen, Y. S.; Magdassi, S.; Shpaisman, H. Continuous nanoparticle assembly by a modulated photo-induced microbubble for fabrication of micrometric conductive patterns. *ACS applied materials & interfaces* **2017,** *9* (50), 44214-44221.

(31) Baffou, G.; Berto, P.; Bermúdez Ureña, E.; Quidant, R.; Monneret, S.; Polleux, J.; Rigneault, H. Photoinduced heating of nanoparticle arrays. *Acs Nano* **2013,** *7* (8), 6478-6488.

(32) Korte, F.; Koch, J.; Chichkov, B. Formation of microbumps and nanojets on gold targets by femtosecond laser pulses. *Applied Physics A* **2004,** *79* (4-6), 879-881.

(33) Namura, K.; Nakajima, K.; Kimura, K.; Suzuki, M. Photothermally controlled Marangoni flow around a micro bubble. *Applied Physics Letters* **2015,** *106* (4), 043101.

(34) Namura, K.; Nakajima, K.; Suzuki, M. Quasi-stokeslet induced by thermoplasmonic Marangoni effect around a water vapor microbubble. *Scientific reports* **2017,** *7* (1), 1-8.

(35) Zhang, Q.; Pang, Y.; Schiffbauer, J.; Jemcov, A.; Chang, H.-C.; Lee, E.; Luo, T. Light-guided surface plasmonic bubble movement via contact line de-pinning by in-situ deposited plasmonic nanoparticle heating. *ACS Applied Materials & Interfaces* **2019,** *11* (51), 48525-48532.

(36) Hu, M.; Petrova, H.; Hartland, G. V. Investigation of the properties of gold nanoparticles in aqueous solution at extremely high lattice temperatures. *Chemical physics letters* **2004,** *391* (4-6), 220-225.

(37) Lapotko, D. Plasmonic nanoparticle-generated photothermal bubbles and their biomedical applications. *Nanomedicine* **2009,** *4* (7), 813-845.

(38) Boulais, E. t.; Lachaine, R. m.; Meunier, M. Plasma mediated off-resonance plasmonic enhanced ultrafast laser-induced nanocavitation. *Nano letters* **2012,** *12* (9), 4763-4769.

(39) Lukianova-Hleb, E. Y.; Volkov, A. N.; Lapotko, D. O. Laser pulse duration is critical for the generation of plasmonic nanobubbles. *Langmuir* **2014,** *30* (25), 7425-7434.

(40) Fu, X.; Chen, B.; Tang, J.; Zewail, A. H. Photoinduced nanobubble-driven superfast diffusion of nanoparticles imaged by 4D electron microscopy. *Science advances* **2017,** *3* (8), e1701160.

(41) Lee, E.; Huang, D.; Luo, T. Ballistic Supercavitating Nano Swimmer Driven by Single Gaussian Beam Optical Pushing and Pulling Forces. *arXiv preprint arXiv:1908.05987* **2019**.

(42) Fujii, S.; Kobayashi, K.; Kanaizuka, K.; Okamoto, T.; Toyabe, S.; Muneyuki, E.; Haga, M.-a. Manipulation of single DNA using a micronanobubble formed by local laser heating on a Au-coated surface. *Chemistry letters* **2009,** *39* (2), 92-93.

(43) Roy, B.; Arya, M.; Thomas, P.; Jürgschat, J. K.; Venkata Rao, K.; Banerjee, A.; Malla Reddy, C.; Roy, S. Self-assembly of mesoscopic materials to form controlled and continuous patterns by thermo-optically manipulated laser induced microbubbles. *Langmuir* **2013,** *29* (47), 14733-14742.

(44) Yamamoto, Y.; Tokonami, S.; Iida, T. Surfactant-Controlled Photothermal Assembly of Nanoparticles and Microparticles for Rapid Concentration Measurement of Microbes. *ACS Applied Bio Materials* **2019,** *2* (4), 1561-1568.

(45) Nishimura, Y.; Nishida, K.; Yamamoto, Y.; Ito, S.; Tokonami, S.; Iida, T. Control of submillimeter phase transition by collective photothermal effect. *The Journal of Physical Chemistry C* **2014,** *118* (32), 18799-18804.

(46) Namura, K.; Imafuku, S.; Kumar, S.; Nakajima, K.; Sakakura, M.; Suzuki, M. Direction control of quasi-stokeslet induced by thermoplasmonic heating of a water vapor microbubble. *Scientific reports* **2019,** *9* (1), 4770.

(47) Setoura, K.; Ito, S.; Miyasaka, H. Stationary bubble formation and Marangoni convection induced by CW laser heating of a single gold nanoparticle. *Nanoscale* **2017,** *9* (2), 719-730.

(48) Wang, Y.; Zaytsev, M. E.; The, H. L.; Eijkel, J. C.; Zandvliet, H. J.; Zhang, X.; Lohse, D. Vapor and gas-bubble growth dynamics around laser-irradiated, water-immersed plasmonic nanoparticles. *ACS nano* **2017,** *11* (2), 2045-2051.

(49) Uwada, T.; Fujii, S.; Sugiyama, T.; Usman, A.; Miura, A.; Masuhara, H.; Kanaizuka, K.; Haga, M.-a. Glycine crystallization in solution by cw laser-induced microbubble on gold thin film surface. *ACS applied materials & interfaces* **2012,** *4* (3), 1158-1163.

(50) Baral, S.; Green, A. J.; Livshits, M. Y.; Govorov, A. O.; Richardson, H. H. Comparison of vapor formation of water at the solid/water interface to colloidal solutions using optically excited gold nanostructures. *ACS nano* **2014,** *8* (2), 1439-1448.

(51) Zhang, Q.; Neal, R. D.; Huang, D.; Neretina, S.; Lee, E.; Luo, T. Surface Bubble Growth in Plasmonic Nanoparticle Suspension. *arXiv preprint arXiv:1912.11097* **2019**.

(52) Baigl, D. Photo-actuation of liquids for light-driven microfluidics: state of the art and perspectives. *Lab on a Chip* **2012,** *12* (19), 3637-3653.

(53) Hao, Y.; Zhang, Y.; Prosperetti, A. Mechanics of gas-vapor bubbles. *Physical review fluids* **2017,** *2* (3), 034303.

(54) Baffou, G.; Polleux, J.; Rigneault, H.; Monneret, S. Super-heating and micro-bubble generation around plasmonic nanoparticles under cw illumination. *The Journal of Physical Chemistry C* **2014,** *118* (9), 4890-4898.

(55) Storhoff, J. J.; Elghanian, R.; Mucic, R. C.; Mirkin, C. A.; Letsinger, R. L. One-pot colorimetric differentiation of polynucleotides with single base imperfections using gold nanoparticle probes. *Journal of the American Chemical Society* **1998,** *120* (9), 1959-1964.

(56) Hurst, S. J.; Lytton-Jean, A. K.; Mirkin, C. A. Maximizing DNA loading on a range of gold nanoparticle sizes. *Analytical chemistry* **2006,** *78* (24), 8313-8318.

(57) Jonstrup, A.; Fredsøe, J.; Andersen, A. DNA hairpins as temperature switches, thermometers and ionic detectors. *Sensors* **2013,** *13* (5), 5937-5944.

(58) Huang, J.; Su, X.; Li, Z. Enzyme-and label-free amplified fluorescence DNA detection using hairpin probes and SYBR Green I. *Sensors and Actuators B: Chemical* **2014,** *200*, 117-122.

(59) Owczarzy, R.; Tataurov, A. V.; Wu, Y.; Manthey, J. A.; McQuisten, K. A.; Almabrazi, H. G.; Pedersen, K. F.; Lin, Y.; Garretson, J.; McEntaggart, N. O. IDT SciTools: a suite for analysis and design of nucleic acid oligomers. *Nucleic acids research* **2008,** *36* (suppl_2), W163-W169.

(60) Qin, Z.; Bischof, J. C. Thermophysical and biological responses of gold nanoparticle laser heating. *Chemical Society Reviews* **2012,** *41* (3), 1191-1217.

Supplementary information

Biocompatible Direct Deposition of Functionalized Nanoparticles using Shrinking Surface Bubble

Seunghyun Moon[1], Qiushi Zhang[1], Dezhao Huang[1], Satyajyoti Senapati[2], Hsueh-Chia Chang[1,2], Eungkyu Lee[1*] and Tengfei Luo[1,2,3*]

[1]Department of Aerospace and Mechanical Engineering, University of Notre Dame, Notre Dame, USA

[2]Department of Chemical and Biomolecular Engineering, University of Notre Dame, Notre Dame, USA

[3]Center for Sustainable Energy of Notre Dame (ND Energy), University of Notre Dame, Notre Dame, USA.

[*]Corresponding to: elee18@nd.edu, tluo@nd.edu,

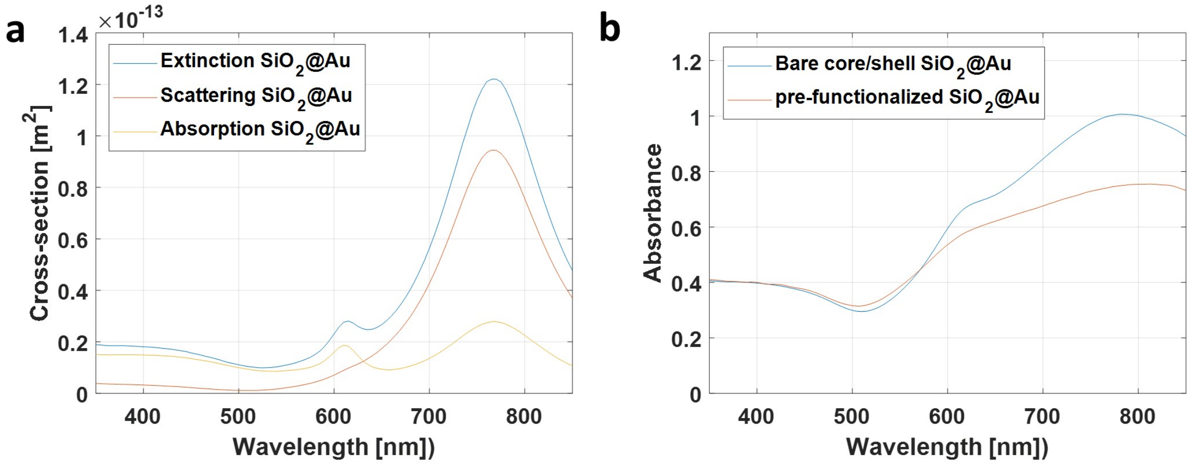

Figure S1. (a) Calculated scattering cross-section for bare core-shell AuNPs. **(b)** The absorbance spectra of bare Au NPs and functionalized AuNPs measured in the suspension using UV-Vis equipment (V-670, Jasco). The peak absorption wavelength is about 785 nm, which can effectively absorb our 800 nm laser irradiation.

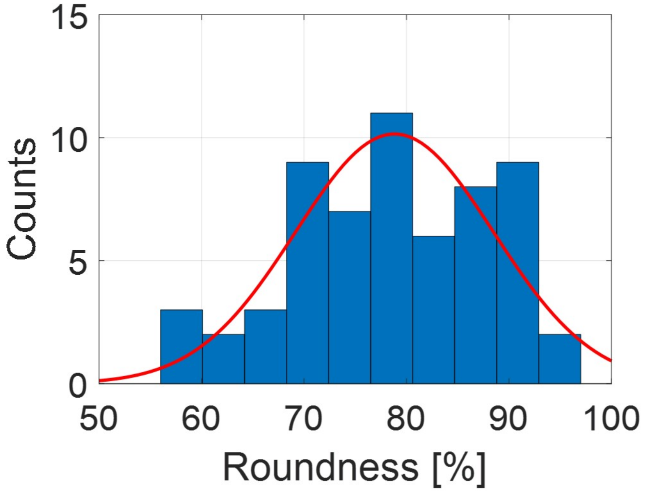

Figure S2. Roundness histogram and normal distribution curve that show the distribution of all data of OD 0.75, 0.32 and 0.15.

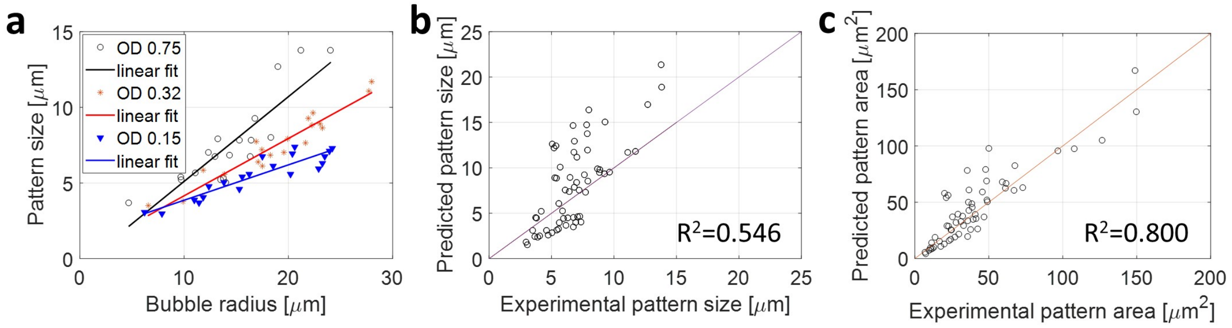

Figure S3. (a) The correlation between pattern size and bubble radius. **(b)** A parity plot for the reduced dimension that compares experimental data against predicted data. We collapse all data by scaling them with the respective slopes of the fit curves of (a), and this yield a general relationship between deposited spot size, bubble size and AuNP concentration as shown in Eq. S1. (c) A parity plot for pattern area. The predicted data of pattern area were obtained from Eq. S2.

The prediction model for the pattern size is as follows:

$$z_1(x,y) = 1.16x_1y + 0.45, \qquad if\ x_1\mathrm{y} > 0 \tag{S1}$$

where, z_1, x_1 and y are pattern size, bubble radius and optical density, respectively. And the prediction model for the pattern area is as follows:

$$z_2(x,y) = 0.03x_2\mathrm{y} + 2.1, \qquad if\ x_2\mathrm{y} > 0 \tag{S2}$$

where, z_2 and x_2 are pattern area and surface area of bubble, respectively.

Table S1. Fitting parameters for bubble radius and pattern size shown in Fig. S3a.

OD at 800 nm	Linear fitting		
	Slope	Intercept	R^2
0.75	0.56	-0.5	0.745
0.32	0.38	0.4	0.921
0.15	0.23	1.5	0.846